

A Bifunctional Electrocatalyst based on Ni-porphyrin/Vapor-Grown Carbon Fibres for Oxygen Reduction and Evolution Reactions in Alkaline Media

Ibrahim Elghamry*, Abdulrahman S. Alablan and MAMDOUN E. Abdelsalam

Department of Chemistry, College of Science, King Faisal University, P.O. Box 400 Al-Ahsa, 31982, Saudi Arabia.

*E-mail: ielghamry@kfu.edu.sa & elghamry@hotmail.com

Received: 10 June 2022 / Accepted: 23 July 2022 / Published: 10 September 2022

Looking for affordable and competent bifunctional electrocatalysts for oxygen evolution reaction (OER) and oxygen reduction reaction (ORR) is imperative for widespread fuel cells and metal-air batteries. Metalloporphyrins have gained considerable attention owing to remarkable catalytic characteristics. Herein, we investigate the catalytic performance of a composite catalyst comprising nickel- 5,10,15,20-tetra(*p*-thioanisole) porphyrin complex (Ni-TPSMe-P) and vapor grown carbon fibres (VGCFs) towards both the OER and ORR. A simple approach is adopted to synthesis the targeted Ni-TPSMe-P. Several spectroscopic techniques, including NMR, FT-IR, UV-Vis and MS are used to confirm the formation of the target catalyst structurally. Also, kinetic parameters such as overpotential (η), Tafel slope, onset potential, the average number of electrons transferred and peroxides yield are used to evaluate the catalytic activity towards the OER, and ORR . The composite catalyst demonstrates OER activity at a current density of 10 mA cm⁻² with an overpotential of 400 mV and Tafel slope of 130 mV dec⁻¹. In addition, the composite catalyst shows high catalytic activity towards the ORR with an average number of electrons of 3.60, onset potential of 0.82 V and peroxide yield of 22%. The bifunctional index (BI) is used to evaluate the bifunctional activity towards the OER and ORR, which is found to be 0.92 V. These outcomes suggest that, the synthesized nickel porphyrin has an outstanding bifunctional characteristic towards the OER and ORR, which is an important merit for energy conversion systems, such as metal-air battery and regenerative fuel cells.

Keywords: Bifunctional electrocatalyst; Nickel Porphyrin; Oxygen Evolution Reaction (OER); Oxygen Reduction Reaction (ORR); Composite Catalyst; Vapor grown carbon fibres (VGCFs).

1. INTRODUCTION

The deterioration of the environment owing to the extensive use of depletable carbon-based energy resources, e.g., fossil fuels, has motivated researchers to find clean and sustainable alternatives

[1–3]. Electrochemistry-based devices, such as metal-air-batteries and fuel cells have received great attention as phenomenal alternatives [4,5]. The oxygen reactions, including oxygen evolution (OER) oxygen reduction (ORR) and hydrogen reactions (either evolution or oxidation HER/HOR), are indispensable key reactions in these devices [6,7]. Nevertheless, the oxygen reactions (OER/ORR) suffer from elevated overpotentials due to the sluggish kinetics; therefore, electrocatalysts must be inevitably used to expedite these processes [8,9]. In general, electrocatalysts employed for the OER are less active towards the ORR and vice versa [7]. For example, noble metal-based electrocatalysts, such as IrO_2 and RuO_2 , are competent at catalyzing the OER, but they have inferior catalytic activity towards the ORR. On the other side, Pt-based electrocatalysts have been reported as the state-of-art for the ORR, but they exhibit poor performance towards the OER [10,11]. Furthermore, noble metal-based electrocatalysts suffer from scarcity and exorbitant cost, which hamper the widespread use in electrochemical energy conversion systems. Thereupon, it is of great importance to develop cost-effective and efficient OER/ORR bifunctional electrocatalysts based on non-precious metals [12,13]. Several efforts have been made to develop efficient and potent OER or/and ORR electrocatalysts based on earth-abundant and low-cost transition metals to replace the noble metal-based electrocatalysts. For example, cobalt-based (Co_3O_4) and manganese-based electrocatalysts (MnO_2) have been intensively investigated as the OER and ORR electrocatalysts owing to their affordability and abundance [14–18]. Nevertheless, metal oxides' catalytic activity has been slightly suppressed due to the low electrical conductivity, low surface area, and the tendency to agglomerate, which diminished their capabilities of catalyzing the multistep process involved in the OER and ORR [15,19]. These challenges, however, have been relatively alleviated by incorporating carbon additives, e.g., CNTs and graphene with cobalt oxides [18,20]. For instance, Kim Y. B. *et. al.*, successfully managed to grow (Co_3O_4) on MWCNTs and investigated its bifunctionality towards the OER/ORR. The outcomes suggested that the composite catalyst exhibited an admirable catalytic performance with a bifunctional index of 0.72V [21]. Perovskites including $\text{La}_{0.6}\text{Ca}_{0.4}\text{MnO}_3$, $\text{Ba}_{0.5}\text{Sr}_{0.3}\text{Co}_{0.8}\text{Fe}_{0.2}\text{O}_3$, LaNiO_3 and $\text{La}_{0.6}\text{Ca}_{0.4}\text{CoO}_3$ are other choices to replace noble metal-based electrocatalysts, which also exhibited a bifunctional characteristics with high catalytic activity towards the OER/ORR [22–25].

Another class of materials which are based on organometallic compounds, such as metalloporphyrins and metal corrole, have also captivated considerable attention due to their structures tunability and ability to harvest light, degrade peroxide, transfer electron, and activate oxygen [26–30]. Porphyrin-based electrocatalysts have been widely utilized to electrocatalyze several reactions, e.g., HER, OER, and ORR [29,31–35]. For example, Cao *et al.* have studied the electrocatalytic activity of a water soluble Cu(II) tetrakis(4-N-methylepyridyle)porphyrin towards the OER in neutral aqueous solutions. The outcomes suggested that, the catalyst exhibited a good performance with minimized overpotential [36]. Also, Q. Zhang *et.al.*, studied the electrocatalytic activity of several transition metals of porphyrin framework (POF) supported on graphene towards the ORR in alkaline condition. The results revealed that, cobalt-porphyrin framework delivered the best catalytic activity with ($E_{1/2}$) of 810 mV *vs* RHE [37]. On the other hand, the utilization of porphyrin-based compounds as bifunctional electrocatalysts for OER/ORR is rarely reported in the literature. Marianov *et al.* have investigated the electrocatalytic activity of Mn tetraphenylporphyrin (Mn-TTP) with different immobilization techniques towards both ORR and OER. The catalyst was covalently anchored to the carbon substrate through

electro-reduction of the diazonium salt. Whereas the Mn-TTP was non-covalently immobilized on the substrate *via* drop casting technique. It was found that the covalent immobilization of the Mn-TTP is more efficient towards the ORR, while the OER was found to be less sensitive to the attachment method [38]. Furthermore, Tang *et al.* have reported the use of a molecular-based electrocatalyst for the OER and ORR. The catalyst is comprising Ni-/Co-porphyrin multilayers grown *via* layer-by-layer (LBL) on reduced graphene oxide (rGO). The outcomes suggested that, the catalyst has considerable catalytic performance towards both of the OER and ORR reactions with a decreased overpotential of 330 mV at 10 mA cm⁻² and an onset potential of 0.84 V *vs* RHE for the OER and ORR, respectively [39].

Herein, we report the bifunctionality of the composite catalyst containing nickel porphyrin and Vapor-grown Carbon Fibres (VGCFs) for the OER/ORR in alkaline solution. The nickel porphyrin was prepared as reported in the literature [40,41]. The synthesized nickel porphyrin has been structurally confirmed using spectroscopic techniques (¹H-NMR, FT-IR, UV-Vis, and MS). The elemental compositions of the composite hybrid catalyst was characterized by energy-dispersive X-ray spectroscopy (EDS). The electrocatalytic performance towards the OER/ORR was evaluated by voltammetric techniques.

2. EXPERIMENTAL

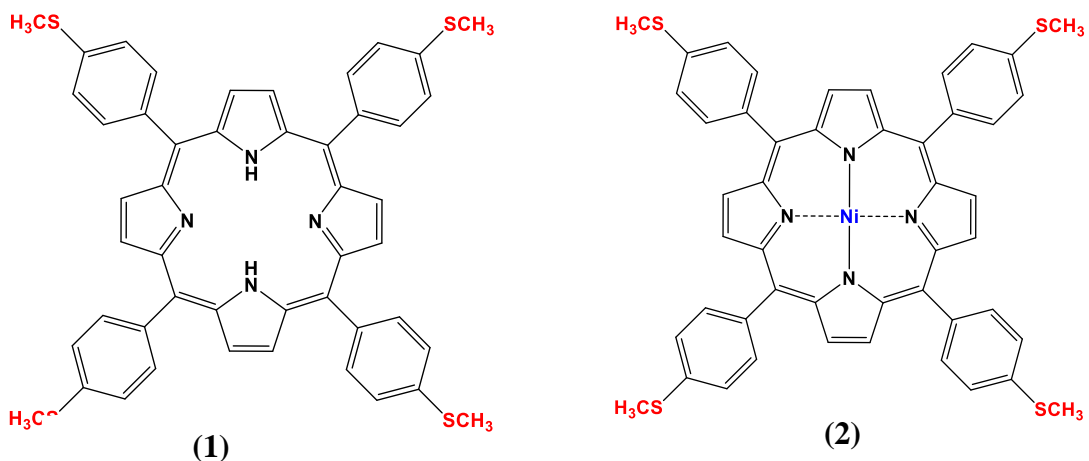
2.1. Chemicals and Materials

Vapor grown carbon fibres (VGCFs) with high electrical conductivity was obtained from Showa Denko USA, Inc. The specific surface area of the fibre is 13 m²/g, and the single fibre specific resistance is 1x10⁻⁴ Ω cm. Solvents and chemicals were procured from Sigma-Aldrich and are directly used without any further purifications. All solutions were prepared utilizing deionized water (18.2 MΩ cm).

2.2. Synthesis of 5,10,15,20- tetra (*p*-thioanisole) porphyrin and its nickel complex.

The 5,10,15,20- tetra (*p*-thioanisole) porphyrin (TPSMe-P) was prepared using the same method reported in the literature [33,40]. In this approach, the pyrrole was reacted with an aldehyde in the presence of an acid catalyst to produce porphyrin. Then, the nickel porphyrin was synthesized by reacting the free base porphyrin with the nickel salt. Scheme S1 displays the synthesis route of the selected porphyrins. The 5,10,15,20- tetra (*p*-thioanisole) porphyrin was prepared by adding a mixture of pyrrole (1) (1 ml, which is equivalent to 14.9 mmol) to 4-(methylthio) benzaldehyde (2) (1.8 ml, which is equivalent to 14.8 mmol). Dimethylformamide (DMF) (10 ml) was utilized as a solvent. The mixture was raised to 100 °C under argon atmosphere. Afterwards, *p*-toluenesulfonic acid (PTSA) (2.82 g, which is equivalent to 16.37 mmol) was added, then the temperature of the reaction mixture was raised to 140 °C, and kept constant for an hour to yield a dark violet colour solution. Thereafter, the violet solution was added to a mixture of cooled water and triethylamine (H₂O/TEA 95: 5 v/v) and left for 30 min. The solution was kept stirring until a solid dark violet of crude freebase porphyrin (3) was precipitated. This precipitate was subjected to filtration, washing several times with water, drying with air, purified by column chromatography (CHCl₃/CH₃OH 99:1 v/v) and crystallized from CHCl₃/CH₃OH. Subsequently,

the synthesis of the nickel 5,10,15,20- tetra (*p*-thioanisole) porphyrin complex was accomplished by reacting the yielded free base porphyrin with nickel acetate. Typically, a mixture of the prepared free base porphyrin (100 mg, 0.09 mmol) and an excess of nickel acetate (0.3 mmol) was dissolved in DMF (5 ml). The reaction mixture was gradually raised to 100 °C under argon (Ar) atmosphere for 3 hours. After that, the mixture was left to cool to room temperature, and poured into cooled water. The solid product was collected by filtration, washed several times by water, air-dried, purified by column chromatography (CHCl₃/CH₃OH 99:1 v/v) and crystallized from CHCl₃/CH₃OH. The nickel porphyrin was obtained in almost quantitative yield. Scheme 1 represents the structure of both the 5,0,15,20- tetra (*p*-thioanisole) porphyrin (TPSMe-P) (1) and nickel 5,10,15,20- tetra (*p*-thioanisole) porphyrin (Ni-TPSMe-P) (2).



Scheme 1. The structure of 5,10,15,20- tetra (*p*-thioanisole) porphyrin (TPSMe-P) (1) and nickelate 5,10,15,20-tetra(*p*-thioanisole) porphyrin (Ni-TPSMe-P) (2).

2.3. Preparation of Nickel Porphyrin composite Catalyst

A composite catalyst was prepared by dispersing a 10 mg of the VGCFs in 500 µl isopropanol (IPA) using the ultrasonic bath for 20 minutes. Thereafter, 20 mg of Ni-TPSMe-P was added to the dispersion and subjected to the second round of ultrasonication for 20 min. Then, 50 µl of nafion oil (5% in water) was added to the mixture followed by the last round of ultrasonication for 30 min to produce a slurry of nickel porphyrin and vapor grown carbon fibres. The glassy carbon electrode (GCE) of 3 mm diameter was modified by drop-casting a 20 µL of the ink on its surface. Then, the electrode was dried first at room temperature and then transferred to the drying oven to be baked at 50 °C for 30 min. In this work, the abbreviation Ni-TPSMe-P/VGCFs will be used to denote the composite catalyst.

2.4. Measurements

The structure of the composite catalyst was investigated using field-emission scanning electronic microscopy (FE-SEM, Model JEOL JSM 5410, Japan) coupled with the Energy Dispersive X-ray

Spectroscopy (EDS). The SEM measurements were recorded using a working distance of 10.3 ± 0.6 mm and an accelerating voltage of 15 kV. The secondary electron detector (SED) was used to recorded images. The energy dispersive X-ray spectroscopy (EDS) was performed using X-Max 80 mm² detectors. BRUKER Nuclear Magnetic Resonance 850 MHT spectrometer was utilized to measure the ¹H-NMR spectra of the Ni-TPSMe-P using CDCl₃. Infrared (FTIR) spectra were obtained through an Agilent Technologies Cary 630 FTIR spectrometer. The MS spectra were obtained using Shimadzu (QP-2010 PULS) mass spectrometer. The UV/Vis spectra were recorded on GENESYS 10 s UV-vis Spectrophotometer.

Electrochemical measurements were performed using a SP150e bipotentiostat (Bio-Logic SAS) configured with electrochemical impedance module. The system was driven by the Bio-Logic Ec-Lab software. The measurements were carried out in a conventional three-electrode cell. The modified GCE with the Ni-TPSMe-P/VGCFs was utilized as a working electrode. The counter electrode was made of a graphite rod. The reference electrode was Ag/AgCl/KCl (sat.) with a Luggin probe positioned near the electrode surface. The electrochemical impedance spectroscopy (EIS) measurements were carried out in the frequency range from 100 KHz to 10 mHz. The amplitude of the sinusoidal signal was 5 mV peak-to-peak at the open circuit potential. The rotating ring disk electrode (RRDE) measurement was carried out with an ALS rotation controller. The RRDE consisted of a glassy carbon disk (4 mm diameter) and a platinum ring of inner and outer diameters of 5 and 7 mm, respectively. The auxiliary (CE) and reference electrodes (RE) were graphite rod electrode and Ag/AgCl/KCl (sat.), respectively. The collection efficiency (N_c) of the RRDE was calculated to be 42%. The electrochemical measurements were conducted at ambient temperature in 0.1 M KOH (pH = 13) solution. The solution was either saturated with O₂ or Ar. The potential of the working electrode was measured with respect to the reference electrode (Ag/AgCl/KCl (sat.)), then was converted to the reversible hydrogen electrode (RHE) according to equation 1:[41]

$$E_{\text{RHE}} = E_{\text{Ag/AgCl/KCl(sat.)}} + 0.197 \text{ V} + (0.0591 \text{ pH}) \quad (1)$$

3. RESULTS AND DISCUSSION

3.1. Spectroscopic Characterization

The spectroscopic techniques (¹H-NMR, UV/Vis, FT-IR and MS) were employed to confirm the structure of the synthesized porphyrins. Fig. 1. shows the ¹H-NMR spectrum for nickel porphyrin in CD₃Cl. The signal that appeared at 2.42 ppm is attributed to the protons of the methyl groups. Signals at 7.25 and 8.1 ppm, is assigned to the protons of thioanisole ring. The signal appeared at 8.9 ppm, is ascribable to the protons on the *beta*-position of the porphyrin skeleton. Similar spectrum was observed for the free base porphyrin, except the appearance of one signal at -2.52 ppm, which could be correlated to the inner protons of the porphyrin ring (N-H). Additionally, UV/Vis spectroscopy investigation were previously reported to confirm the structure of both the free base and the nickel porphyrins [42]. The outcomes obtained are consistent with the previously reported literature, which indicated that, the

intercalation of a metal ion in the porphyrin ring would slightly distort the porphyrin ring's planarity [43,44].

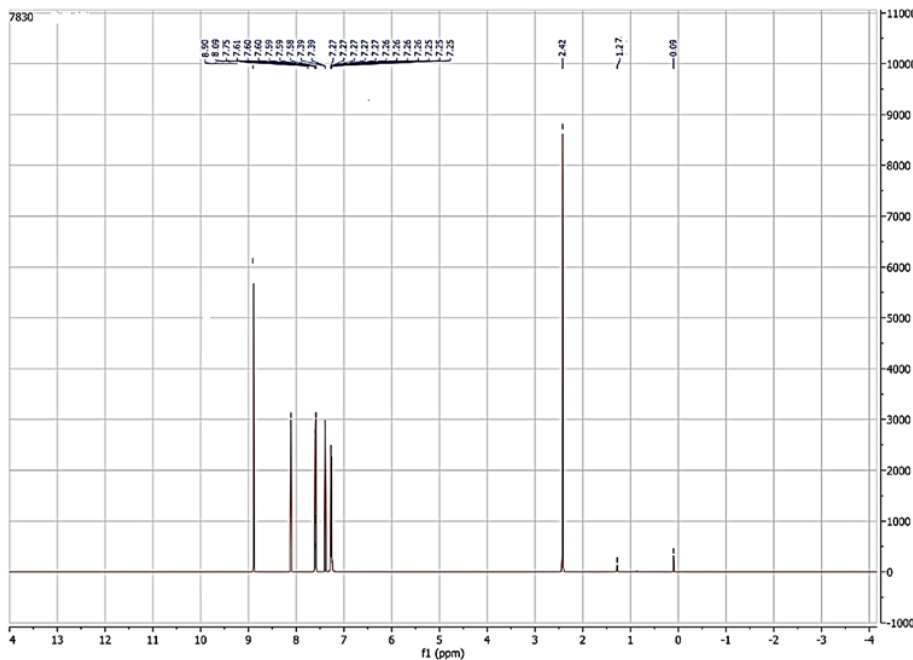


Figure 1. ^1H -NMR spectrum of the nickel porphyrin in deuterated chloroform.

Furthermore, the FT-IR was further utilized to confirm the formation of synthesized porphyrin, as shown in Fig. 2. The free base porphyrin revealed three distinctive peaks for N-H vibrational modes at 3434, 1134 and 966 cm^{-1} , which are correlated to in-phase stretching, in-plane and out of the plane deformation respectively. However, these peaks have been disappeared after the intercalation of the Ni ion at the center of the porphyrin, confirming the formation of the target Nickel porphyrin complex.

The SEM and EDS were employed to confirm the structure and elemental compositions of the composite catalyst. Fig. 3(a) shows SEM image of the Ni-TPSMe-P/VGCFs composite at different magnifications. The VGCFs form a highly conductive network in direct contact of the porphyrin molecules, which could massively promote the electrical conductivity. The porphyrin and VGCFs will be strongly adhered together via π - π interaction. The enhanced conductivity is expected to contribute in accelerating the kinetics of the OER and ORR. The SEM instrument was coupled with EDX analyzer to confirm the elemental analysis of the composite catalyst. Fig. 3(b). shows the EDX chart with peaks for C, F, N, S, O and Ni. Fig. 3(c). demonstrates the EDS mapping of C, N, S, F, O, and Ni. The C originated from the VGCFs as well as from the porphyrin skeleton. The N came from porphyrin structure, while S originated from the porphyrin structure and the nafion oil. The O and F came from the nafion oil (the binder). Finally, the Ni originated from the nickel-porphyrin. These results confirm the formation of the target composite catalyst.

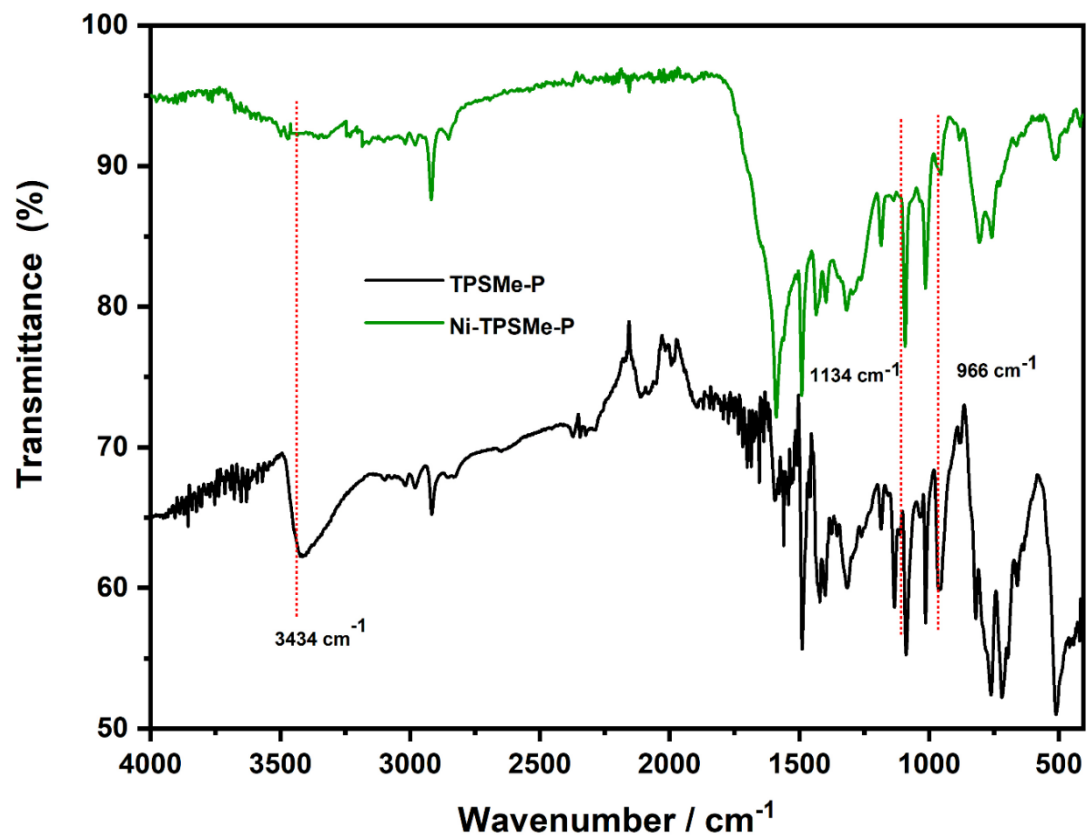
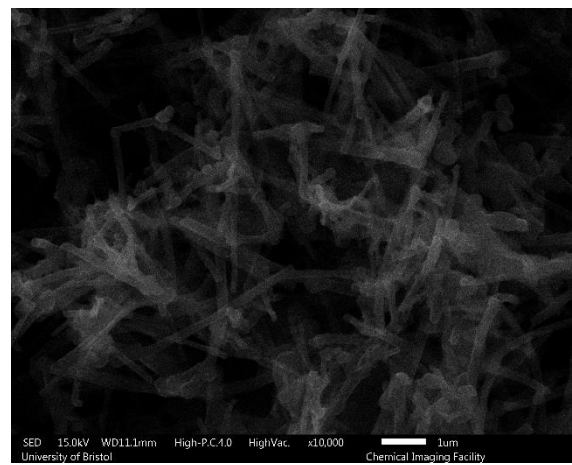


Figure 2. FT-IR spectra of the freebase porphyrin (black curve) and the Ni porphyrin (green curve). The positions of the N-H bands are indicated as dashed lines at 3434, 1134 and 966 cm⁻¹

a



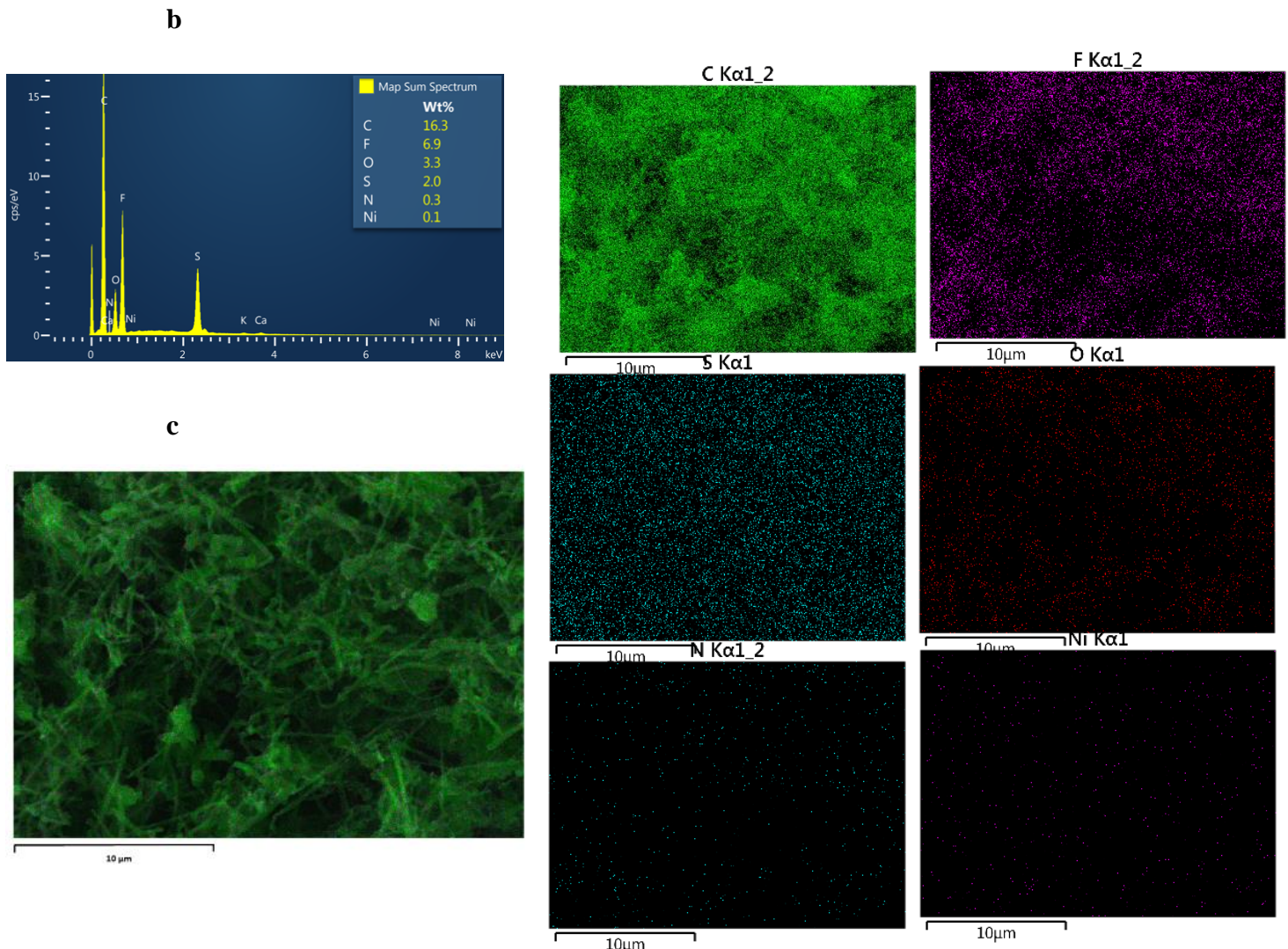


Figure 3. SEM images (a), EDX peaks (b) and EDS maps (c) for Ni-TPSMe-P/VGCFs composite catalyst showing the uniform distribution of C, F, S, N, O and Ni elements

3.2. The Electrochemical Characterization of the Composite Catalyst

First, the composite catalyst was tested by cycling a GCE coated the Ni-TPSMe-P/VGCFs catalyst in a solution containing 0.05M $\text{K}_4\text{Fe}(\text{CN})_6$ and 0.5M KNO_3 ($\text{pH} = 7$) at different sweep rates, as shown in Fig. 4(a). A plot of the current density versus the square root of the scan rate gives a straight line, which is characteristic of a diffusion-controlled process. In addition, a linear sweep voltammogram was recorded at a very slow rate (10 mV/s) for the GCE coated the Ni-TPSMe-P/VGCFs catalyst in 0.1 M KOH, as shown in Fig. 4(b). The coverage of the GCE with nickel porphyrin (Γ) was quantified by the integration of the area under the oxidation peak, and calculated using the following equation 2 [45].

$$\Gamma = \frac{Q}{nF} \quad (2)$$

Where the charge, the number of involved electrons and Faraday's constant are denoted as Q , n ($n=1$) and F (96485 C mol^{-1}), respectively. The surface coverage under the oxidation peak of the nickel porphyrin was found to be $8.2 \times 10^{16} \text{ Ni atoms/cm}^2$.

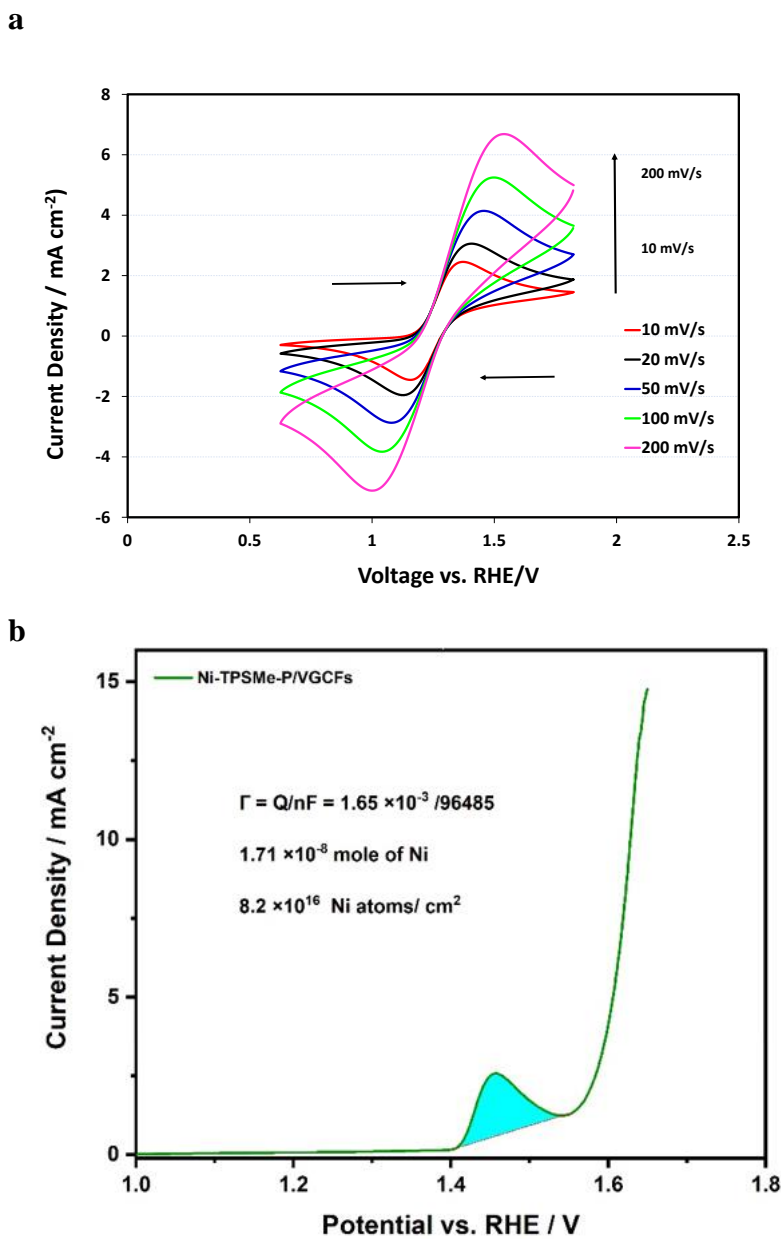


Figure 4. Cyclic voltammograms recorded at various scan rates for GCE coated with Ni-TPSMe-P/VGCFs in aqueous solution of 10 mM $\text{K}_4\text{Fe}(\text{CN})_6$ and 1M KNO_3 (a), the integration area under the oxidation peak for GCE coated with Ni-TPSMe-P/VGCFs electrode in Ar-saturated 0.1 M KOH solution at a scan rate of 10 mV s⁻¹ (b).

The electrical conductivities (R_s) of the CGE coated with Ni-TPSMe-P/VGCFs and Ni-TPSMe-P were measured through the electrochemical impedance spectroscopy (EIS). Fig. 5 (a-b) elucidates Nyquist plots for the investigated electrodes in 0.1 M KOH saturated with argon.

The shape of the Nyquist plots for the of Ni-TPSMe-P/VGCFs shows ion diffusion region at high frequency with a slope of 45° , which is attributed to a porous composite electrode. The porosity is inherited from the VGCFs.

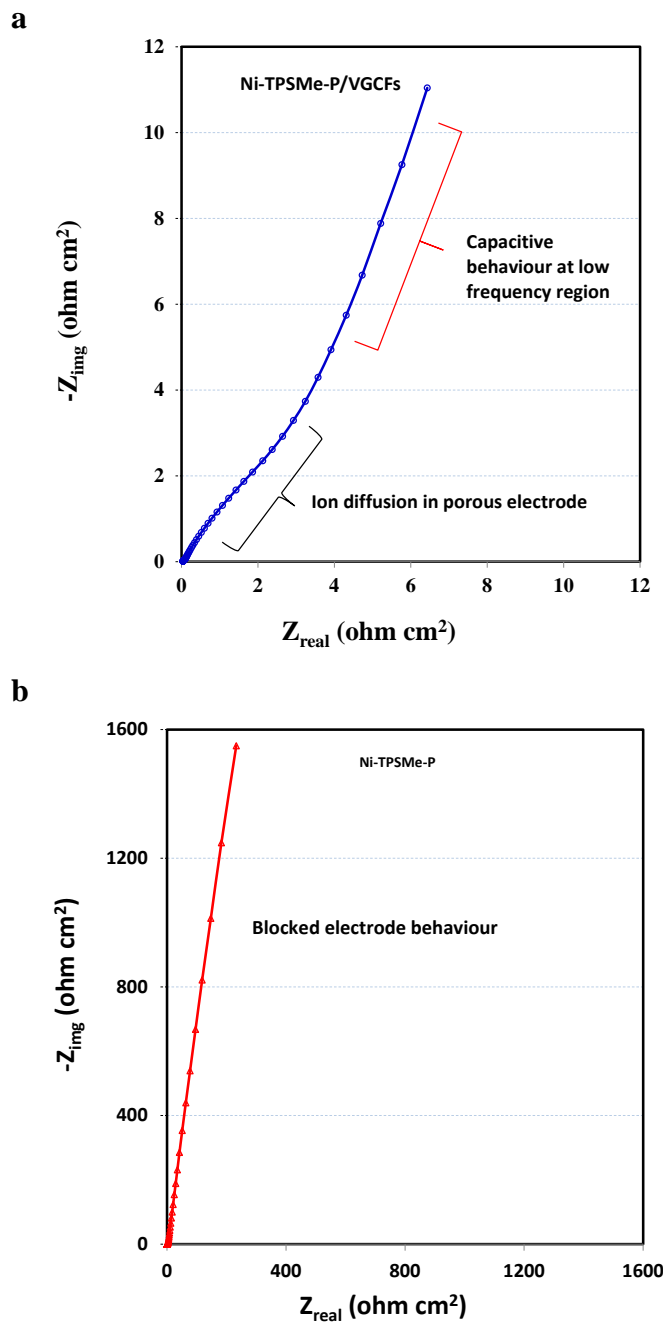


Figure 5. Nyquist plots for GCE coated with Ni-TPSMe-P/VGCFs (a), and Ni-TPSMe-P (b). The EIS experiment was recorded in a solution of 1 M KOH. the frequency scanned from 100 kHz to 10 mHz using a signal of amplitude 5 mV peak-to-peak at the open circuit potential.

While at low frequency the plot exhibits capacitive behavior. On the other hand, the Ni-TPSMe-P displays blocked electrode behavior [46]. The intercept of the plot with the x-axis (Z_{real} ohm cm^2)

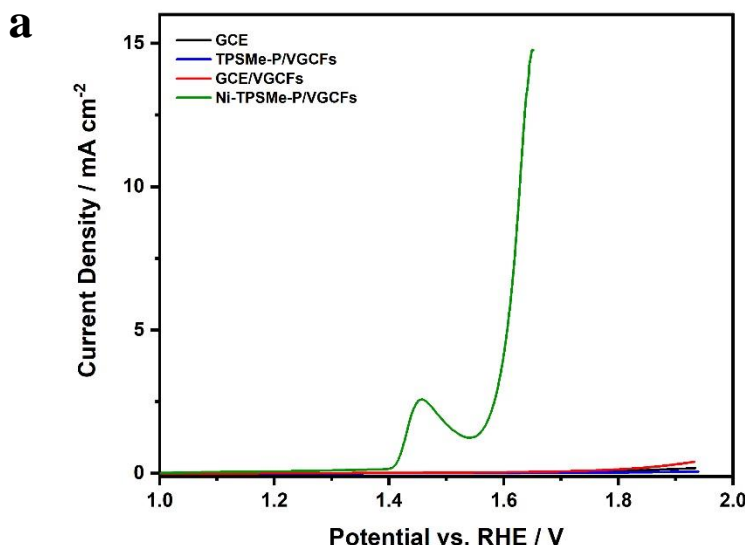
gives the series resistance (R_s). The R_s includes several types of resistance; such as the intrinsic resistance of porphyrin and VGCFs, the contact resistance between the composite catalyst and the GCE, and the electrolyte solution resistance. The R_s values for Ni-TPSMe-P/VGCFs, and Ni-TPSMe-P were found to be 0.1, and $0.9 \Omega \text{ cm}^2$, respectively. The elevated R_s value for the Ni-TPSMe-P indicates the poor electrical conductivity of the porphyrin, which was alleviated by adding VGCFs to the Ni-TPSMe-P.

3.3. The Electrocatalytic Activity of The Ni-TPSMe-P/VGCFs towards the OER

In order to assess the electrocatalytic performance of the Ni-TPSMe-P/VGCFs towards the OER, the measurements were carried out in 0.1 M KOH solution using rotating disk electrode (RDE) at a scan rate of 10 mVs^{-1} and a rotation rate of 1600 rpm. The RDE was deliberately implemented to allow the removal of the produced oxygen on the composite catalyst's surface. Fig. 6a shows the linear sweep voltammograms (LSVs) recorded for the GCE modified with VGCFs, TPSMe-P/VGCFs and Ni-TPSMe-P/VGCFs. The onset potential and the overpotential were used as indicator parameters for assessing the electrocatalytic activity for the investigated electrodes. As clearly shown in Fig. 6a, the electrocatalytic activity of GCE after the modification with Ni-TPSMe-P/VGCFs has drastically ameliorated with a very low onset potential of 1.51 V when compared with the GCE, VGCFs and TPSMe-P/VGCFs, that displayed more positive onset potentials of 1.75, 1.72 and 1.83 V, respectively. Fig. 6b. elucidates a summary of the onset potential of the investigated electrodes. The overpotential of the Ni-TPSMe/VGCFs was calculated using the following equation [47].

$$\eta = E - E^\circ \quad (3)$$

Where E is the practical potential at the working electrode, whilst E° is the standard potential for the OER (1.23V vs RHE).



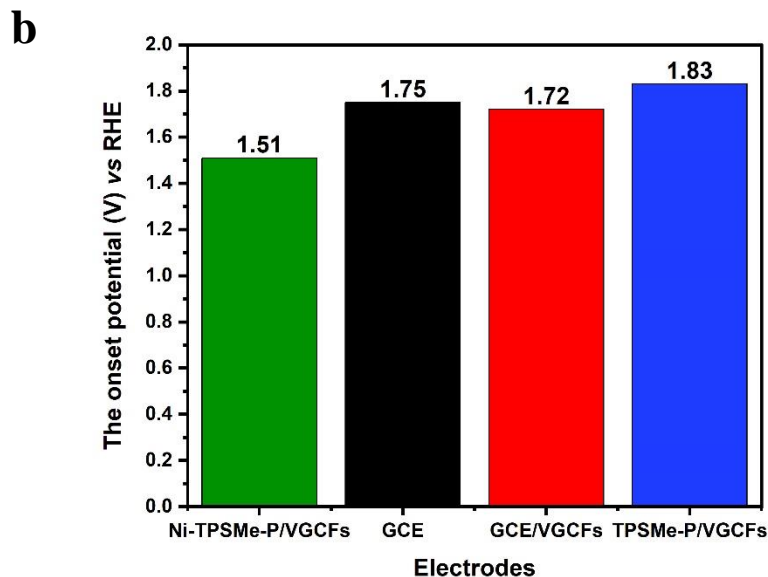


Figure 6. Comparative RDE-LSVs of GCE (black curve) and GCE modified with VGCFs (red curve), TPSMe-P/VGCFs (blue curve) and Ni-TPSMe-P/VGCFs (green curve) in Ar-saturated 0.1 M KOH at a sweep rate of 10 mV s⁻¹ and rotation rate of 1600 rpm (a), the OER onset potential vs RHE for the investigated GCE, VGCFs, TPSMe-P/VGCFs and Ni-TPSMe-P/VGCFs electrodes (b).

The calculated overpotential for the Ni-TPSMe-P/VGCFs at 10 mA cm⁻² was found to be 400 mV. Having observed such catalytic activity with the Ni-TPSMe-P/VGCFs indicates that the inserted nickel ion at the porphyrin center functions as a catalytically active site for the evolution of O₂.

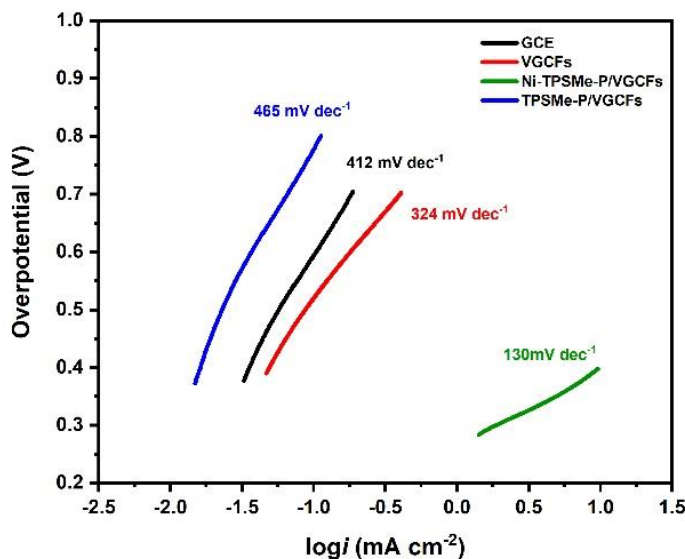


Figure 7. Tafel slopes for the GCE and GCEs modified with VGCFs, TPSMe-P/VGCFs and Ni-TPSMe-P/VGCFs.

To further assess the performance of the investigated electrode, the Tafel slope was also employed. Fig. 7 illustrates the Tafel slope for the investigated GCE, VGCFs, TPSMe-P/VGCFs and Ni-TPSMe-P/VGCFs electrodes. As illustrated in Fig. 7, the Tafel slope for the Ni-TPSMe-P/VGCFs is 130 mV dec^{-1} while the GCE, VGCFs and TPSMe-P/VGCFs were found to be $412, 324$ and 465 mV dec^{-1} , respectively. This value of Tafel slope for the Ni-TPSMe-P/VGCFs indicates a high electrocatalytic activity along with fast kinetic reaction as compared to GCE, VGCFs and TPSMe-P/VGCFs electrodes.

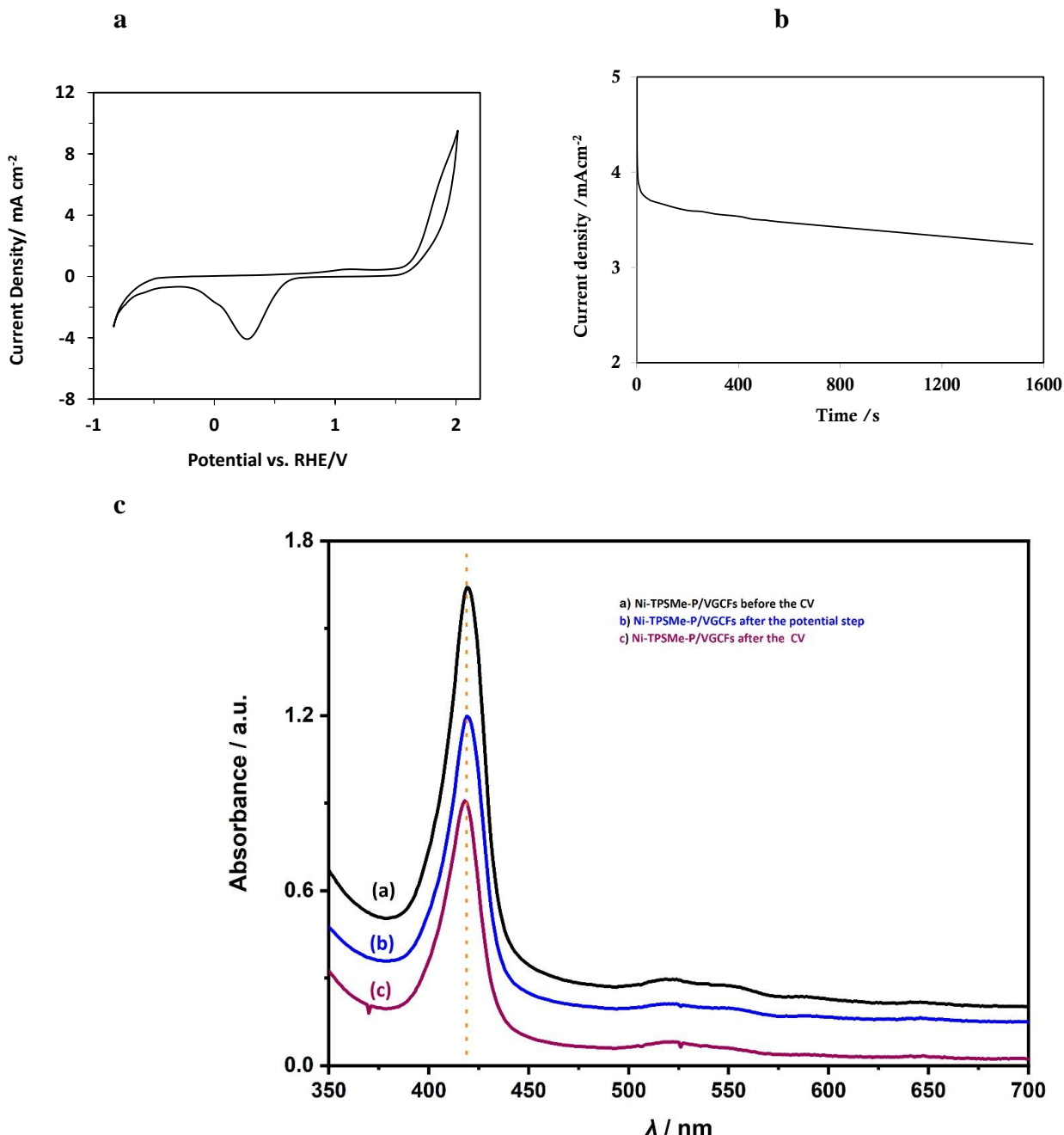


Figure 8. Full CV to show the OER and ORR CV recorded for GCE modified with Ni-TPSMe-P/VGCFs catalyst at a scan rate of 20 mV s^{-1} in Ar-saturated 0.1 M KOH solution (a), current density versus time curve; the potential was stepped from 0 to 1.8 V versus RHE (b), UV/Vis for the catalyst before recording the CV, after recording the CV, and after recording the potential step (c)

The stability of the GCE coated with a composite catalyst of Ni-TPSMe-P/VGCFs was investigated by recording cyclic voltammograms in 0.1 M KOH, as shown in Fig 8(a). The potential range of the CV was selected to include both the OER and ORR. Also, a chronoamperogram was recorded in the same solution. A step potential, 1. 8 V, was particularly selected to match the value, which is required to drive the OER and produce significant current density at the electrode surface. The produced Faradaic current was recorded against time, as shown in Fig 8 (b). The composite catalysts maintained its high efficiency towards the OER as indicated by the slight decrease in the value of the current density for about 25 min. Evolution of O₂ gas bubbles was observed at the surface of the composite catalyst. When the rate of the gas bubbles massively increased the composite catalyst starts to delaminate off the electrode surface hence significant reduction in catalytic activity was observed. UV/Vis Spectra, shown in figure 8(c), were recorded for the Ni-TPSMe-P/VGCFs in dichloromethane (DCM) before recording the CV, after recording the CV and after recording the potential step. All spectra revealed a strong Soret band at the wavelength ($\lambda_{\text{max}}=424$ nm), confirming the stability of the Ni porphyrin complex.

3.4. The Electrocatalytic Activity of the Ni-TPSMe-P/VGCFs towards the ORR

Figure. 9 represents the RDE of the GCE and GCE modified with Ni-TPSMe-P/VGCFs in 0.1 M KOH O₂-saturated solution at the rotation speed of 1600 rpm and a scan rate of 10 mV s⁻¹.

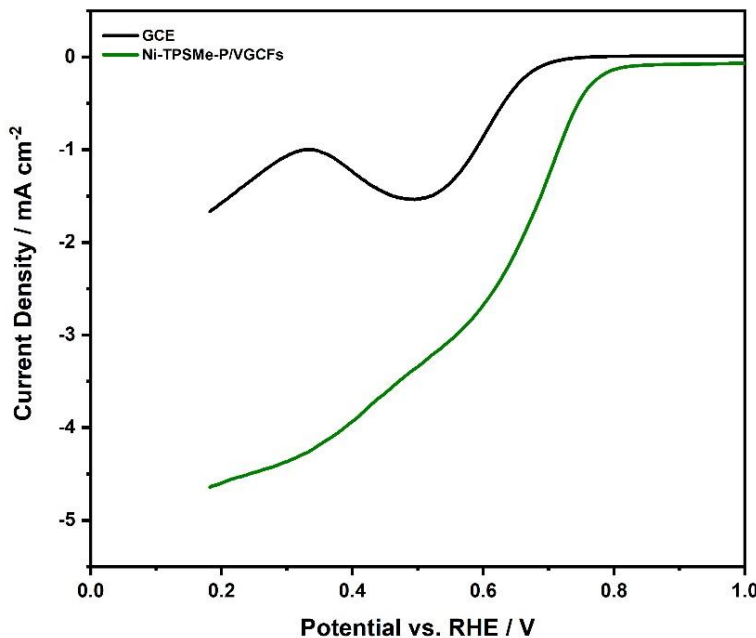


Figure 9. RDE-LSV for unmodified GC and Ni-TPSMe-P/VGCFs electrodes in O₂-saturated 0.1 M KOH solution at 1600 rpm at scan rate of 10 mV s⁻¹.

As displayed in Fig. 9, the onset potential of the GCE prior to the modification with the Ni-TPSMe-P/VGCFs is more cathodic with the value of 0.70 V *vs* RHE. However, after modifying the

GCE with the Ni-TPSMe-P/VGCFs, the catalytic activity towards the ORR was dramatically enhanced along with a positive shift of the onset potential to be 0.82 V *vs* RHE. The enhancement in the current density and the onset potential are good indicators to the excellent catalytic activity. The selectivity of the Ni-TPSMe-P/VGCFs towards the ORR was previously reported by calculating the average number of electrons as well as the peroxide species yield [42]. The calculated peroxide species was found to be 22.5% and average number of the involved electrons was found to be 3.55, indicating that, the Ni-TPSMe-P/VGCFs tends to favor the reduction of the oxygen *via* four-electron pathway.

3.5. The OER/ORR bifunctional Activity of the Ni-TPSMe/VGCFs

Bifunctional electrocatalysts are crucial for energy conversion systems including metal-air-batteries and regenerative fuel cells.

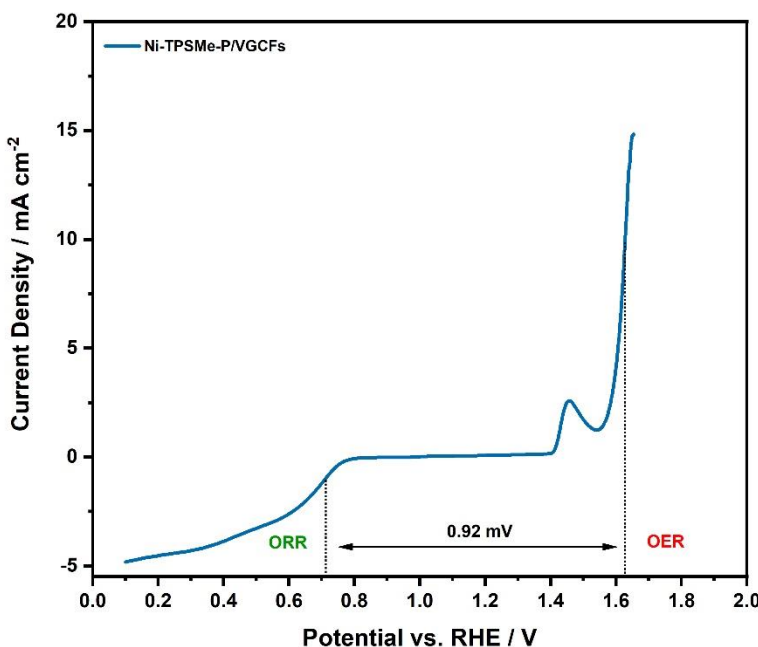


Figure 10. Evaluation of oxygen catalysis (OER/ORR) activity of Ni-TPSMe-P/VGCFs using RDE at rotation rate of 1600 rpm and scan rate of 10 mV s⁻¹.

Generally, the assessment of the bifunctional electrocatalytic activity is based on the bifunctional index or called peak separation (BI); since the (BI) is defined as the difference between the potential required to achieve 10 mA cm⁻² for the OER and -1 mA cm⁻² for the ORR. The BI can be calculated using equation 4 [48].

$$\Delta E = E_{\text{OER at } 10 \text{ mA cm}^{-2}} - E_{\text{ORR at } -1 \text{ mA cm}^{-2}} \quad (4)$$

When the value of the (BI) is low, this implies a good bifunctional electrocatalytic activity. Fig. 10. represents the evaluation of OER/ORR bifunctional activity of Ni-TPSMe-P/VGCFs using RDE at a rotation rate of 1600 rpm and a scan rate of 10 mV s⁻¹. As shown in Fig. 10 the Ni-TPSMe-P/VGCFs exhibited a small (BI) of 0.92 mV. These outcomes suggested that, the fabricated composite (Ni-TPSMe-P/VGCFs) has good catalytic performance towards both OER and ORR. Table 1 represents parameters for comparison of the fabricated electrocatalyst with other reported catalysts. Although the catalytic activity of Ni-TPSMe-P/VGCFs towards the OER and ORR is still not as high as precious metal alloys, it may be deemed significant because it is a noble metal-free electrocatalyst.

Table 1. Comparison between the Ni-TPSMe-P/VGCFs with other electrocatalysts as OER and ORR catalyst.

Electrocatalysts	OER potential (V) vs RHE @ 10 mA/cm ²	η_{OER} (mV) @ 10 mA/cm ²	ORR onset potential (V) vs RHE	ΔE (V)*	Ref.
Co@CoO@Co ₃ O ₄ -N/C	1.66	430	0.84	0.85	[49]
Co ₁ Ni ₁ @N-C	1.73	500	0.91	0.87	[50]
Mn oxide	1.77	540	0.85	0.99	[51]
Pt/C (20%)	2.02	790	1.01	1.09	[51]
CoFe ₂ O ₄ (crystalline)	1.72	490	0.81	0.98	[52]
Co ₃ O ₄	1.66	430	0.83	0.97	[53]
Co-porphyrin on 1/CNTs	1.65	407	0.83	0.93	[54]
Co-porphyrin on 2/CNTs	1.7	480	0.78	1.02	[54]
Fe porphyrin	1.7	490	0.93	0.78	[55]
Ni-TPSMe-P/VGCFs	1.63	400	0.82	0.92	This work

* The bifunctional index was calculated at current density of 10 mA cm⁻² for the OER and -1 mA cm⁻² for the ORR

4. CONCLUSION

A one pot-multistep approach was utilized to synthesize the free base porphyrin (TPSMe-P) and nickel porphyrin (Ni-TPSMe-P). Spectroscopic techniques (NMR, FT-IR, UV-Vis and MS) confirmed the intercalation of nickel at the center of the porphyrin ring. Incorporating VGCFs with the Ni-TPSMe-P to form a composite catalyst improved the electrical conductivity and the overall catalytic activity. The high catalytic activity of the composite catalyst towards the OER was evaluated in terms of overpotential and was found to be 400 mV with a Tafel slope of 130 mV dec^{-1} . Whereas the catalytic activity towards the ORR was assessed by the onset potential, the average number of electrons and peroxide species of 0.82 V, 3.60 and 22 %, respectively. The bifunctional index of the composite catalyst towards the OER/ORR was found to be 0.92 V. These outcomes could pave the way to consider Ni-TPSMe-P/VGCFs as a potential material for energy conversion systems.

COMPLIANCE WITH ETHICAL STANDARDS

CONFLICT OF INTEREST

We would like to declare that there is no conflict of interest.

ACKNOWLEDGEMENT

This work was supported by the Deanship of Scientific Research, Vice Presidency for Graduate Studies and Scientific Research, King Faisal University, Saudi Arabia grant number (GRANT823).

References

1. A. Mehboob, S.R. Gilani, A. Anwar, A. Sadiqa, S. Akbar, J. Patujo, *Journal of Applied Electrochemistry* (2021).
2. K. Sasidharachari, S. Yoon, K.Y. Cho, *Journal of Applied Electrochemistry*, 50 (2020) 907–915.
3. M.A. Garcia-Contreras, P. Hosseini-Benhangi, E.L. Gyenge, *Journal of Applied Electrochemistry*, 49 (2019) 281–290.
4. K. Kim, M.P. Kim, W.-G. Lee, *New Journal of Chemistry*, 41 (2017) 8864–8869.
5. K.-S. Lee, S. Maurya, Y.S. Kim, C.R. Kreller, M.S. Wilson, D. Larsen, S.E. Elangovan, R. Mukundan, *Energy & Environmental Science*, 11 (2018) 979–987.
6. X. Chen, H. Zhang, X. Li, *Molecular Catalysis*, 502 (2021) 111383.
7. H. Li, Z. Guo, X. Wang, *Journal of Materials Chemistry A*, 5 (2017) 21353–21361.
8. Y.-C. Lu, Z. Xu, H.A. Gasteiger, S. Chen, K. Hamad-Schifferli, Y. Shao-Horn, *Journal of the American Chemical Society*, 132 (2010) 12170–12171.
9. K. Fujimoto, Y. Ueda, D. Inohara, Y. Fujii, M. Nakayama, *Electrochimica Acta*, 354 (2020) 136592.
10. X. Wang, Z. Liao, Y. Fu, C. Neumann, A. Turchanin, G. Nam, E. Zschech, J. Cho, J. Zhang, X. Feng, *Energy Storage Materials*, 26 (2020) 157–164.
11. A. Samanta, A. Ghatak, S. Bhattacharyya, C.R. Raj, *Electrochimica Acta*, 348 (2020) 136274.
12. J. Zhu, X. Jiang, Y. Yang, Q. Chen, X.-X. Xue, K. Chen, Y. Feng, *Physical Chemistry Chemical Physics*, 21 (2019) 22939–22946.

13. J. Zhang, M. Zhang, L. Qiu, Y. Zeng, J. Chen, C. Zhu, Y. Yu, Z. Zhu, *Journal of Materials Chemistry A*, 7 (2019) 19045–19059.
14. S. Liu, L. Li, H.S. Ahn, A. Manthiram, *Journal of Materials Chemistry A*, 3 (2015) 11615–11623.
15. A. Ajiaz, J. Masa, C. Rösler, W. Xia, P. Weide, A.J.R. Botz, R.A. Fischer, W. Schuhmann, M. Muhler, *Angewandte Chemie International Edition*, 55 (2016) 4087–4091.
16. L. Xu, Q. Jiang, Z. Xiao, X. Li, J. Huo, S. Wang, L. Dai, *Angewandte Chemie International Edition*, 55 (2016) 5277–5281.
17. B.S. Yeo, A.T. Bell, *Journal of the American Chemical Society*, 133 (2011) 5587–5593.
18. Y. Liang, Y. Li, H. Wang, J. Zhou, J. Wang, T. Regier, H. Dai, *Nature Materials*, 10 (2011) 780–786.
19. F. Cheng, Y. Su, J. Liang, Z. Tao, J. Chen, *Chemistry of Materials*, 22 (2010) 898–905.
20. T.-C. Tsai, G.-M. Huang, C.-W. Huang, J.-Y. Chen, C.-C. Yang, T.-Y. Tseng, W.-W. Wu, *Analytical Chemistry*, 89 (2017) 9671–9675.
21. M.S. Ahmed, B. Choi, Y.-B. Kim, *Scientific Reports*, 8 (2018) 2543.
22. S. Malkhandi, B. Yang, A.K. Manohar, A. Manivannan, G.K.S. Prakash, S.R. Narayanan, *The Journal of Physical Chemistry Letters*, 3 (2012) 967–972.
23. W.G. Hardin, D.A. Slanac, X. Wang, S. Dai, K.P. Johnston, K.J. Stevenson, *The Journal of Physical Chemistry Letters*, 4 (2013) 1254–1259.
24. M. Bursell, M. Pirjamali, Y. Kiros, *Electrochimica Acta*, 47 (2002) 1651–1660.
25. J.-I. Jung, M. Risch, S. Park, M.G. Kim, G. Nam, H.-Y. Jeong, Y. Shao-Horn, J. Cho, *Energy & Environmental Science*, 9 (2016) 176–183.
26. J. Schindler, S. Kupfer, L. Zedler, M. Wächtler, S. Gräfe, A.A. Ryan, M.O. Senge, B. Dietzek, *ChemPhysChem*, 17 (2016) 3480–3493.
27. W. Zhang, W. Lai, R. Cao, *Chemical Reviews*, 117 (2017) 3717–3797.
28. S. Wannakao, T. Maihom, K. Kongpatpanich, J. Limtrakul, V. Promarak, *Physical Chemistry Chemical Physics*, 19 (2017) 29540–29548.
29. X. Li, H. Lei, L. Xie, N. Wang, W. Zhang, R. Cao, *Accounts of Chemical Research*, 55 (2022) 878–892.
30. X. Li, X.-P. Zhang, M. Guo, B. Lv, K. Guo, X. Jin, W. Zhang, Y.-M. Lee, S. Fukuzumi, W. Nam, R. Cao, *Journal of the American Chemical Society*, 143 (2021) 14613–14621.
31. Y. Han, Y. Wu, W. Lai, R. Cao, *Inorganic Chemistry*, 54 (2015) 5604–5613.
32. S.M. Golabi, A. Nozad, *Electroanalysis*, 16 (2004) 199–209.
33. I. Elghamry, S.S. Ibrahim, M. Abdelsalam, Y. Al-Faiyz, M. Al-Qadri, *International Journal of Electrochemical Science*, 13 (2018) 10233–10246.
34. B.B. Beyene, S.B. Mane, C.H. Hung, *Journal of the Electrochemical Society*, 165 (2018) H481–H487.
35. B. Mondal, P. Sen, A. Rana, D. Saha, P. Das, A. Dey, *ACS Catalysis*, 9 (2019) 3895–3899.
36. Y. Liu, Y. Han, Z. Zhang, W. Zhang, W. Lai, Y. Wang, R. Cao, *Chemical Science*, 10 (2019) 2613–2622.
37. C. Zhao, B. Li, J. Liu, J. Huang, Q. Zhang, *Chinese Chemical Letters*, 30 (2019) 911–914.
38. A.N. Marianov, Y. Jiang, *ACS Sustainable Chemistry and Engineering*, 7 (2019) 3838–3848.
39. J. Sun, H. Yin, P. Liu, Y. Wang, X. Yao, Z. Tang, H. Zhao, *Chemical Science*, 7 (2016) 5640–5646.
40. I. Elghamry, L.F. Tietze, *Journal of Heterocyclic Chemistry*, 42 (2005) 503–508.
41. X. Shang, J.-Q. Chi, S.-S. Lu, B. Dong, X. Li, Y.-R. Liu, K.-L. Yan, W.-K. Gao, Y.-M. Chai, C.-G. Liu, *International Journal of Hydrogen Energy*, 42 (2017) 4165–4173.
42. I. Elghamry, A.S. Alablan, M.A. Alkhalifah, M.E. Abdelsalam, *Journal of The Electrochemical Society*, 168 (2021) 16510.
43. Z. Valicsek, O. Horváth, *Microchemical Journal*, 107 (2013) 47–62.

44. A. Hoshino, Y. Ohgo, M. Nakamura, *Tetrahedron Letters*, 46 (2005) 4961–4964.
45. R.H. Tammam, A.H. Touny, M.E. Abdesalam, M.M. Saleh, *Journal of Electroanalytical Chemistry*, 823 (2018) 128–136.
46. B.T. Mark E. Orazem, *Electrochemical Impedance Spectroscopy*, 2nd Editio, John Wiley & Sons, Inc., (2017) New Jersey.
47. S. Anantharaj, S.R. Ede, K. Karthick, S. Sam Sankar, K. Sangeetha, P.E. Karthik, S. Kundu, *Energy & Environmental Science*, 11 (2018) 744–771.
48. M. Retuerto, F. Calle-Vallejo, L. Pascual, G. Lumbeeck, M.T. Fernandez-Diaz, M. Croft, J. Gopalakrishnan, M.A. Peña, J. Hadermann, M. Greenblatt, S. Rojas, *ACS Applied Materials & Interfaces*, 11 (2019) 21454–21464.
49. G. Xu, G.-C. Xu, J.-J. Ban, L. Zhang, H. Lin, C.-L. Qi, Z.-P. Sun, D.-Z. Jia, *Journal of Colloid and Interface Science*, 521 (2018) 141–149.
50. H. Ning, G. Li, Y. Chen, K. Zhang, Z. Gong, R. Nie, W. Hu, Q. Xia, *ACS Applied Materials & Interfaces*, 11 (2019) 1957–1968.
51. Y. Gorlin, T.F. Jaramillo, *Journal of the American Chemical Society*, 132 (2010) 13612–13614.
52. A. Indra, P.W. Menezes, N.R. Sahraie, A. Bergmann, C. Das, M. Tallarida, D. Schmeißer, P. Strasser, M. Driess, *Journal of the American Chemical Society*, 136 (2014) 17530–17536.
53. T. Maiyalagan, K.A. Jarvis, S. Therese, P.J. Ferreira, A. Manthiram, *Nature Communications*, 5 (2014) 3949.